



# CHORUS

This is the accepted manuscript made available via CHORUS. The article has been published as:

## Prompt and delayed spectroscopy of $^{203}\text{At}$ : Observation of a shears band and a $29/2^{\{+\}}$ isomeric state

K. Auranen *et al.*

Phys. Rev. C **97**, 024301 — Published 2 February 2018

DOI: [10.1103/PhysRevC.97.024301](https://doi.org/10.1103/PhysRevC.97.024301)

# Prompt and delayed spectroscopy of $^{203}\text{At}$ : Observation of a shears band and a $^{29/2^+}$ isomeric state

K. Auranen,<sup>1,2,\*</sup> J. Uusitalo,<sup>1</sup> S. Juutinen,<sup>1</sup> H. Badran,<sup>1</sup> F. Defranchi Bisso,<sup>1</sup> D. Cox,<sup>1</sup> T. Grahn,<sup>1</sup> P.T. Greenlees,<sup>1</sup> A. Herzáň,<sup>1,†</sup> U. Jakobsson,<sup>3,‡</sup> R. Julin,<sup>1</sup> J. Konki,<sup>1</sup> M. Leino,<sup>1</sup> A. Lightfoot,<sup>1</sup> M.J. Mallaburn,<sup>4</sup> O. Neuvonen,<sup>1</sup> J. Pakarinen,<sup>1</sup> P. Papadakis,<sup>1</sup> J. Partanen,<sup>1</sup> P. Rahkila,<sup>1</sup> M. Sandzelius,<sup>1</sup> J. Sarén,<sup>1</sup> C. Scholey,<sup>1</sup> J. Sorri,<sup>1,§</sup> S. Stolze,<sup>1</sup> and Y.K. Wang<sup>5</sup>

<sup>1</sup>*University of Jyväskylä, Department of Physics,*

*P.O. Box 35, FI-40014 University of Jyväskylä, Finland*

<sup>2</sup>*Argonne National Laboratory, Argonne, Illinois 60439, USA*

<sup>3</sup>*Department of Physics, Royal Institute of Technology, SE-10691 Stockholm, Sweden*

<sup>4</sup>*School of Physics and Astronomy, Schuster Building,*

*University of Manchester, Manchester M13 9PL, United Kingdom*

<sup>5</sup>*State Key Laboratory of Nuclear Physics and Technology,*

*School of Physics, Peking University, Beijing 100871, China*

(Dated: January 18, 2018)

Using fusion-evaporation reactions, a gas-filled recoil separator, recoil-gating technique and recoil-isomer decay tagging technique we have extended the level scheme of  $^{203}\text{At}$  ( $N = 118$ ) significantly. We have observed an isomeric [ $\tau = 14.1(3) \mu\text{s}$ ] state with a spin and parity of  $^{29/2^+}$ . The isomeric state is suggested to originate from the  $\pi(h_{9/2}) \otimes |^{202}\text{Po}; 11^- \rangle$  coupling, and it is depopulated through 286-keV  $E2$  and 366-keV  $E3$  transitions. In addition, we have observed a cascade of magnetic dipole transitions which is suggested to be generated by the shears mechanism.

## I. INTRODUCTION

The nuclei close to the magic  $Z = 82$  shell gap are observed to have several interesting nuclear properties and phenomena. These include, but are not limited to, shape coexistence, superdeformed bands, shears bands, and a large variety of low and high-lying isomeric states. Also, sudden changes in spin, parity and deformation of the ground state are observed in this region (See, for example, Refs. [1–3] and references therein). Near the  $N = 126$  shell closure, spherical or nearly spherical shapes can be found in even-mass polonium nuclei. When the neutron number decreases, there is a change to oblate deformed, and later prolate deformed, structure close to neutron midshell ( $N = 104$ ) [4, 5]. As the odd-mass astatine nuclei can be described as an odd proton coupled to an even-mass polonium core, this onset of deformation can be predicted to exist also in astatine nuclei, and indeed the existing spectroscopical studies support this picture (see, for example, Refs. [6–12]).

In the previous study of  $^{203}\text{At}$  [10], around twenty  $\gamma$ -ray transitions were identified, and the level scheme was built up to maximum spin of  $^{23/2^{(-)}}$  and an excitation energy of 1965 keV in the negative parity cascade. Similarly, the level scheme on positive parity side was unambiguously identified up to maximum spin and excitation

energy of  $^{19/2^+}$  and 1942 keV, respectively. However, there is some room for improvements. Above the mentioned excited states, there are a couple of low-energy transitions,  $\Delta$ , which Dybdal *et al.* were not able to identify. In addition, the present level scheme of  $^{203}\text{At}$  is lacking the isomeric  $^{29/2^+}$  state. This state is known in the neighboring astatine isotopes  $^{199,201,205,209,211}\text{At}$  [7, 9, 11, 13, 14], hence one might expect it to exist also in  $^{203}\text{At}$ . Recent studies [9, 15] report observations of a shears band in nearby nuclei  $^{201}\text{At}$  and  $^{204}\text{At}$ , respectively. Therefore,  $^{203}\text{At}$  is a good candidate nucleus for another shears band.

Rotational-like cascades of  $M1$ -type transitions were found in nearly spherical nuclei in the early 1990s. The stunning observable in these cascades was the regularity of the observed  $\gamma$ -ray energy spectrum, it was almost like a superdeformed band. Nowadays more than 50 of these bands have been found mainly in lead and bismuth nuclei ([16] and references therein), but a few examples are also known in other mass regions, for example, in  $^{105}\text{Sn}$  [17],  $^{106,108}\text{Sn}$  [18],  $^{110}\text{Cd}$  [19], and  $^{139}\text{Sm}$  [20]. To date, only four shears bands are known in nuclei heavier than bismuth, these are  $^{201}\text{At}$  [9],  $^{204}\text{At}$  [15],  $^{205}\text{Rn}$  [21] and  $^{206}\text{Fr}$  [15]. Shears bands can be described in detail through the tilted axis cranking covariant density functional theory (TAC-CDFT) [22–25], which enables a description of rotational excitations on the basis of a well-determined covariant density functional. So far, the TAC-CDFT has been successfully used to describe shears bands [23, 26], antimagnetic rotation bands [27, 28], chiral doublet bands [29], linear alpha cluster bands [30], and transitions of nuclear spin orientation [31], and it has demonstrated high predictive power [24, 25]. In particular for  $A \sim 200$  region, the shears bands observed in

\* kauranen@anl.gov

† Present address: Oliver Lodge Laboratory, University of Liverpool, Liverpool L69 7ZE, United Kingdom

‡ Present address: Department of Chemistry - Radiochemistry, P.O. Box 55, FI-00014 University of Helsinki, Finland

§ Present address: University of Oulu, Sodankylä Geophysical Observatory, Tähteläntie 62, FI-99600 Sodankylä, Finland

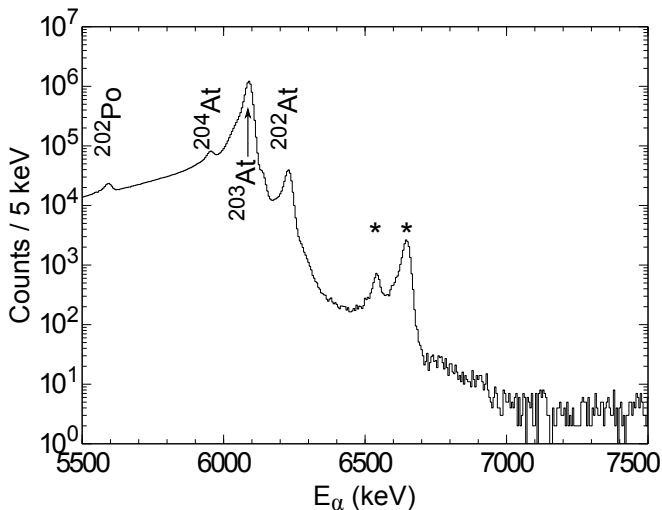


FIG. 1. MWPC-vetoed  $\alpha$ -particle energy spectrum observed in the DSSD obtained with the  $^{48}\text{Ca}(198\text{ MeV}) + ^{159}\text{Tb}$  reaction. Activities marked with an asterisk most likely originate from a contaminant  $^{48}\text{Ti}$  beam, see text for details.

$^{198,199}\text{Pb}$  were well explained with the TAC-CDFT [26].

In this publication we, present an updated level scheme for the  $^{203}\text{At}$  nucleus including the isomeric  $29/2^+$  state and a suggested shears band. The feeding and depopulation of the isomeric state is extracted and compared to the systematics of the neighboring nuclei. Also, a justification for the shears band assignment is discussed.

## II. EXPERIMENTAL DETAILS

The experiment was conducted in the Accelerator Laboratory at the Department of Physics at the University of Jyväskylä, where the K-130 cyclotron provided the used  $^{48}\text{Ca}$  beam with an energy of 198 MeV, a typical intensity of 10 pnA and total irradiation time of 70 h. The beam was guided to a self supporting  $^{159}\text{Tb}$  target with a thickness of  $360\ \mu\text{g}/\text{cm}^2$ . This led, among other reactions, to a fusion-evaporation reaction of  $^{159}\text{Tb}(^{48}\text{Ca},4n)^{203}\text{At}$ . The relative yields for other fusion-evaporation channels may be estimated from the  $\alpha$ -decay energy spectrum presented in Fig. 1. In the high-energy side of the spectrum, one may observe some contaminant  $\alpha$  peaks. If the  $^{48}\text{Ca}$  beam included a contaminant  $^{48}\text{Ti}$  beam component, it would populate  $^{202}\text{Rn}$ ,  $^{203m}\text{Rn}$ ,  $^{199}\text{At}$  and  $^{200m}\text{At}$  nuclei. The  $\alpha$ -particle energies of these nuclei are close to those observed contaminant ones, which are marked with an asterisk in Fig. 1.

Prompt  $\gamma$ -ray transitions at the target position were observed with the JUROGAMII array. In JUROGAMII, there are a total of 24 clover [32] and 15 tapered [33, 34] Compton-suppressed germanium detectors. In this report, we omit the exact value of the angular distribution parameter,  $A_2$  [35]. This is because the observed angular distributions showed some irreg-

ular behavior, which might originate from a misplaced target and/or calibration source. Also, the various isomeric states present in the level scheme (See Sec. IV) make the angular distribution analysis even more challenging. However, a clear ascending ( $A_2 > 0$ ) or descending ( $A_2 < 0$ ) trend was observed for the angular distributions of a previously identified [10] stretched quadrupole or dipole transitions, respectively. Therefore, the sign of the  $A_2$  may be announced.

The gas-filled recoil separator RITU [36, 37] was used to extract the fusion-evaporation residues (later recoils) from the primary beam and other unwanted target-like and beam-like nuclei. At the focal plane of RITU, the recoils were implanted into a  $300\text{-}\mu\text{m}$  thick double-sided silicon strip detector (DSSD), the main instrument of the GREAT spectrometer [38]. The DSSD was surrounded upstream by PINs, an array of 28 silicon detectors in a box arrangement. These charged-particle detector setups were set to detect  $\alpha$  particles and conversion electrons. A planar germanium detector was placed immediately behind the DSSD inside the GREAT vacuum chamber. The planar detector was primarily used for low-energy  $\gamma$  rays and x-rays. An array of three clover detectors was placed in close geometry around the DSSD vacuum chamber to detect  $\gamma$ -ray transitions with higher energies. The peak-to-total ratio of all clover-type detectors was improved through an add-back method. A multiwire-proportional counter (MWPC) was placed between RITU and GREAT. Energy losses to the MWPC and time-of-flights between MWPC and DSSD enabled to distinguish between recoils and scattered beam particles.

Data from all ADC channels were recorded independently using the triggerless total data readout method (TDR) [39]. A 100-MHz clock was used to timestamp all recorded events, and the GRAIN software [40] was used in the data analysis.

## III. TAC-CDFT

It has been found that the pairing correlations should be important in the description of shears bands in the  $A \sim 200$  mass region [26]. Recently, the tilted axis cranking covariant density function theory (TAC-CDFT) with pairing correlations has been developed in Ref. [31] with a monopole force, and later in Ref. [41] with the separable pairing force [42]. Therefore, in the following, the TAC-CDFT with pairing correlations are employed. Furthermore, the successful relativistic density functional PC-PK1 [43] in the particle-hole channel, and the finite range separable pairing force [42] in the particle-particle channel are adopted. As commonly done, the strength of the pairing force is enhanced about 2% to avoid an unphysical collapse of pairing gaps. The relativistic Hartree-Bogoliubov equation is solved in a three-dimensional harmonic oscillator basis in Cartesian coordinates with 12 major shells.

## IV. RESULTS

### A. Isomeric $^{29/2^+}$ state

The level scheme below the isomeric  $^{29/2^+}$  state was constructed mainly based on the  $\gamma\gamma$  coincidences, the angular distribution of prompt  $\gamma$  rays and energy sums. The validity of the level scheme was confirmed by extracting the total transition intensity for each transition at the focal plane  $I_{TR}(FP)$ . The observed transitions are listed in Table I, and the obtained level scheme is presented in Fig. 2. The applicable parts of the level scheme obtained in this study are in agreement with the one suggested earlier [10]. Some details of the analysis are now discussed.

Fig. 3(a) shows the singles energy spectrum of the  $\gamma$  rays observed in the focal-plane clover array within 30  $\mu$ s from the recoil implantation to DSSD. Most of the observed transitions are previously assigned to  $^{203}\text{At}$  [10]. The search time of 30  $\mu$ s corresponds roughly to three times the half-life of the isomeric state of interest. This time condition is applied to all delayed  $\gamma$ -ray and conversion-electron data presented in this work if not stated otherwise. Extraction of the half-life is discussed later in this section. Fig. 3 also shows two examples of  $\gamma\gamma$  coincidence analysis using focal-plane clover detectors, these are presented in panels (b) and (c). In addition to transitions observed in clover detectors, there are a couple of low-energy  $\gamma$  rays, which are only observable in the planar germanium detector placed inside the GREAT vacuum chamber.

Two examples of  $\gamma$ -ray energy spectra observed using the planar detector are presented in Fig. 4. Panel (a) shows the energy spectrum of  $\gamma$  rays in prompt coincidence with the 286 or 309-keV  $\gamma$ -ray transition observed in the focal plane clover array. Panel (b) is the same as (a), but the gate is set to the 411-keV transition. In panel (a) one can observe low-energy transitions with transition energies of 39 and 64 keV. Based on the data obtained in this study it is impossible to fix the ordering of these transitions in the level scheme. However, the intensity analysis dictates  $M1$  and  $E2$  character for the 39 and 64-keV transitions, respectively.

Figs. 3(c) and 4(b) show a coincidence between the 411 and 286-keV transitions. This suggests that there is a weak link transition between the positive and negative parity cascades. A comparison of the  $K_\alpha$  and  $K_\beta$  x-ray intensities in Fig. 4(b) reveals that there is some additional intensity in the peak close to the energy of the astatine  $K_\alpha$  x-ray energy. The total transition intensity of this additional 80-keV transition is comparable to the total transition intensity of the 286-keV transition in Fig. 4(b), if the 80-keV transition is assumed to be of type  $E1$ . In addition, the energy difference between the  $^{25/2^+}$  and the  $^{23/2^-}$  state is 80 keV, hence an  $E1$  transition is placed between them.

The assignments of the  $E2$  and  $E3$  character for the 286- and 366-keV transitions, respectively, are based on

TABLE I. Observed  $\gamma$  rays below the  $^{29/2^+}$  isomeric state in  $^{203}\text{At}$ .  $I_\gamma$  is the relative  $\gamma$ -ray intensity and  $A_2$  is the angular distribution parameter, both are deduced from recoil-gated JUROGAMII data. Transition energy,  $E_\gamma$ , and the total transition intensity,  $I_{TR}(FP)$ , are deduced from the focal-plane clover singles data if not specified otherwise. The internal-conversion coefficients for the calculation of the  $I_{TR}(FP)$  were taken from [44].  $I_{TR}(FP)$  is normalized such that the 286-keV  $\gamma$ -ray transition has an intensity of 100.

$E_\gamma$ (keV)	$I_\gamma$	$I_{TR}(FP)$	$A_2$	$I_i^\pi$	$I_f^\pi$
38.5(2) <sup>a</sup>		130(30) <sup>a</sup>		$(^{21/2^+})^b$	$^{19/2^+b}$
63.5(3) <sup>a</sup>		160(50) <sup>a</sup>		$^{25/2^+b}$	$(^{21/2^+})^b$
80.0(2) <sup>c</sup>		8(2) <sup>c</sup>		$^{25/2^+}$	$^{23/2^-}$
211.9(2)	47.6(15)	58(9)		$^{13/2^+}$	$^{11/2^-}$
223.2(2)	7.5(5) <sup>d</sup>	8.3(12)		$^{13/2^+}$	$^{13/2^-}$
246.5(2)	10.1(6) <sup>e</sup>	31(4)	<0	$^{19/2^+}$	$^{17/2^+}$
254.3(2)	15.4(8) <sup>e</sup>	24(3)	<0	$^{17/2^+}$	$^{15/2^+}$
285.8(2)		115(12)		$^{29/2^+}$	$^{25/2^+}$
308.7(2)	36.3(1.2)	67(7)	<0	$^{19/2^+}$	$^{17/2^+}$
316.5(2)	8.5(6)	11.3(14)	<0	$^{17/2^+}$	$^{15/2^+}$
328.1(2)	15.2(10)	112(12)	<0	$^{23/2^-}$	$^{21/2^-}$
365.8(2)		110(11)		$^{29/2^+}$	$^{23/2^-}$
411.2(2)	41.8(14)	116(11)	>0	$^{21/2^-}$	$^{17/2^-}$
506.9(2)	44(3) <sup>e</sup>	51(6)	<0	$^{15/2^+}$	$^{13/2^+}$
576.5(2)	79(3)	139(15)	>0	$^{17/2^-}$	$^{13/2^-}$
648.6(2)	100(4)	160(20)	>0	$^{13/2^-}$	$^{9/2^-}$
660.0(2)	56(3)	90(10)		$^{11/2^-}$	$^{9/2^-}$
716.4(2)	10.8(4)	8(2)		$^{19/2^+}$	$^{17/2^-}$
761.4(2)	32.2(10)	60(7)	>0	$^{17/2^+}$	$^{13/2^+}$
823.7(2)	10.8(4)	33(4)	>0	$^{17/2^+}$	$^{13/2^+}$
871.8(2)	15.9(5)	41(5)		$^{13/2^+}$	$^{9/2^-}$

<sup>a</sup> Deduced from planar detector data, that is gated with suitable  $\gamma$ -ray transitions observed in the focal-plane clover array.

<sup>b</sup> Ordering of the 39 and 64-keV transitions is not clear. See text for details.

<sup>c</sup> Transition observed indirectly, see text for details. Transition energy is calculated from the energy difference of the 286 and 366-keV transitions. Intensity is from 411-keV (clover) gated planar vs clover  $\gamma\gamma$  data. The number of  $K_\alpha$  x-rays is subtracted based on the number of observed  $K_\beta$  x-rays.

<sup>d</sup> Intensity from the 649-keV gated  $\gamma\gamma$  data. Intensity normalized to the intensity of the 577-keV transition in singles spectrum.

<sup>e</sup> Intensity from the 660-keV gated  $\gamma\gamma$  data. Intensity normalized to the intensity of the 761-keV transition in singles spectrum.

the internal-conversion intensity ratio  $K/L+M+\dots$ . The spectra used in this analysis are presented in Fig. 5(a) and 5(b). For the 286-keV transition the extracted intensity ratio is 0.99(22), which matches with a theoretical [44] ratio of 0.98(3), calculated for a 286-keV  $E2$  transition. Similarly, the deduced ratio of 0.55(8) matches with a theoretical [44] ratio of 0.50(2), calculated for a 366-keV  $E3$  transition. In both spectra there are some transitions overlapping with the transitions of interest, especially the 309-keV transition which overlaps with the 286-keV transition. The number of events in each case were extracted by using a multi-component fit. The validity of this method was confirmed by extracting also the intensity ratio for the 309-keV transition, which agrees with

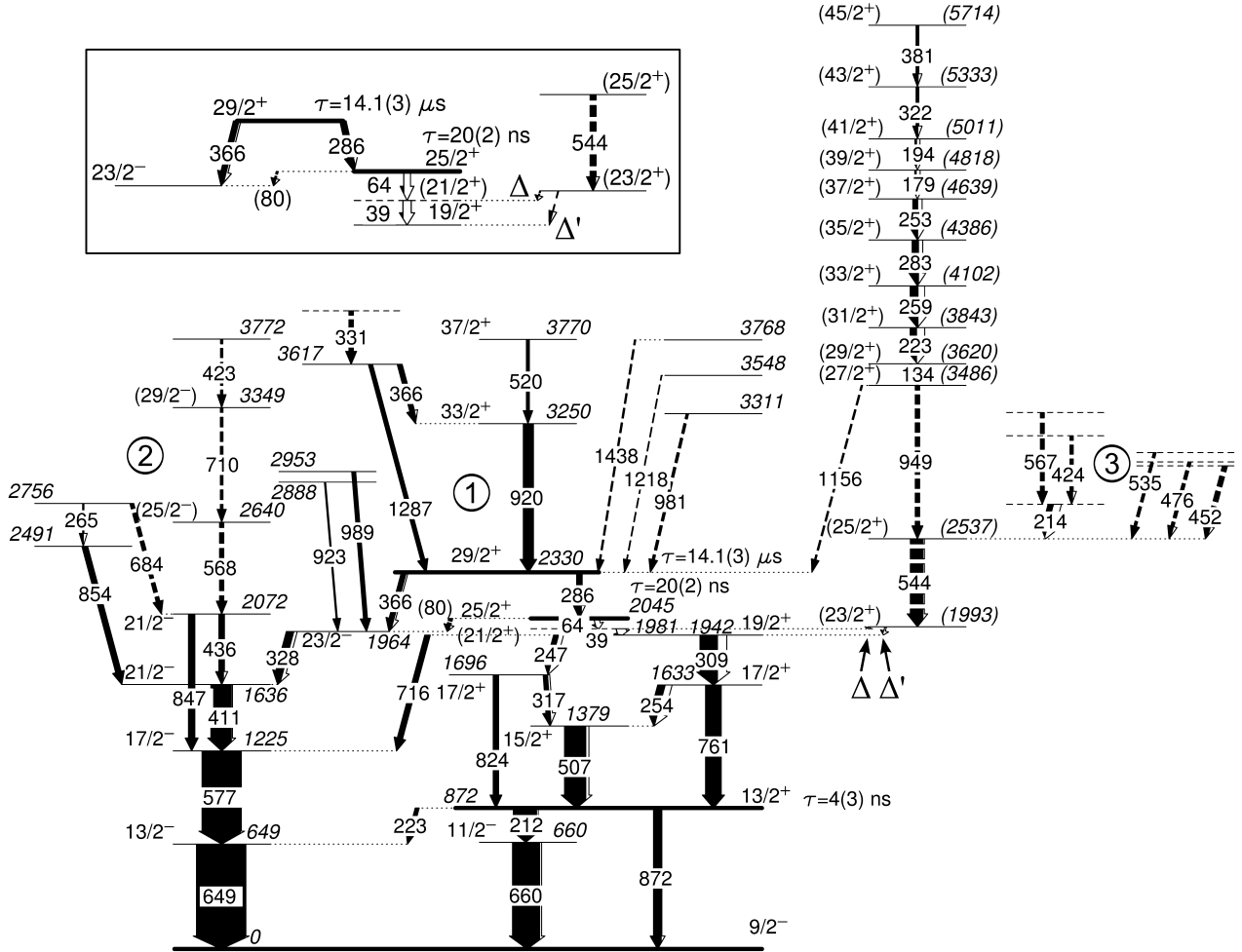


FIG. 2. Partial level scheme of  $^{203}\text{At}$ . The level scheme of the levels connected to the isomeric intruder  $1/2^+$  state is shown in Ref [45]. The purpose of the inset is to clarify the low-energy transitions below the isomeric  $29/2^+$  state. The transitions marked with  $\Delta$  and  $\Delta'$  were not observed, but  $\gamma\gamma$  coincidences suggest that those are present. Energy summing of  $\gamma$  rays suggest a transition energy of 12 keV and 51 keV for  $\Delta$  and  $\Delta'$ , respectively. The circled numbers refer to group number in Table III.

a theoretical [44] estimate calculated for a 309-keV  $M1$  transition. The previous study [10] suggested this character for the 309-keV transition, and the angular distribution of prompt  $\gamma$  rays obtained in this study supports this picture. The theoretical  $K/L+M+\dots$  intensity ratio for a 309-keV  $E1$  transition is nearly equal to the corresponding theoretical ratio of an  $M1$  transition, hence this analysis does not confirm the character of the 309-keV transition. However, this shows that the used fitting method produces reasonable  $K/L+M+\dots$  ratios despite the overlap of the peaks. The contribution of the 212-keV  $L+M+\dots$  conversions to the peak at energy of  $\sim 200$  keV was considered to be negligible. This is reasonable because the 212-keV transition, being of type  $E1$ , has a small total conversion branch and large  $K/L+M+\dots$  ratio.

In Fig. 6 the time distributions between the recoil implantation and the subsequent  $\gamma$  rays depopulating the isomeric state are shown. In panel (a) the 286-keV transition is observed in the planar detector and it must be

in prompt coincidence with the 761-keV  $\gamma$ -ray transition, observed in the focal-plane clover array. Panel (b) is the same, but with transition energies of 366 keV (planar) and 577 keV (clover). The mean lifetimes, extracted using a logarithmic time-scale method [46], are nearly identical, indicating that the 286-keV and 366-keV transitions are from the same isomeric state. The longer-lived component in both distributions are the outcome of random  $\gamma$ -ray coincidences originating, for example, from Compton scattering. The 30  $\mu\text{s}$  time gate was omitted in these lifetime analyses.

The mean lifetime of the  $13/2^+$  and  $25/2^+$  states were extracted through centroid-shift method, which gives lifetimes of 4(3) ns and 20(2) ns, respectively. Selected examples of this analysis are shown in Fig. 7, where the time distributions between two  $\gamma$  rays observed in the focal plane clover array are presented. The time difference between the selected  $\gamma$  rays was taken from the timestamp of each observed  $\gamma$  ray. The dashed distributions

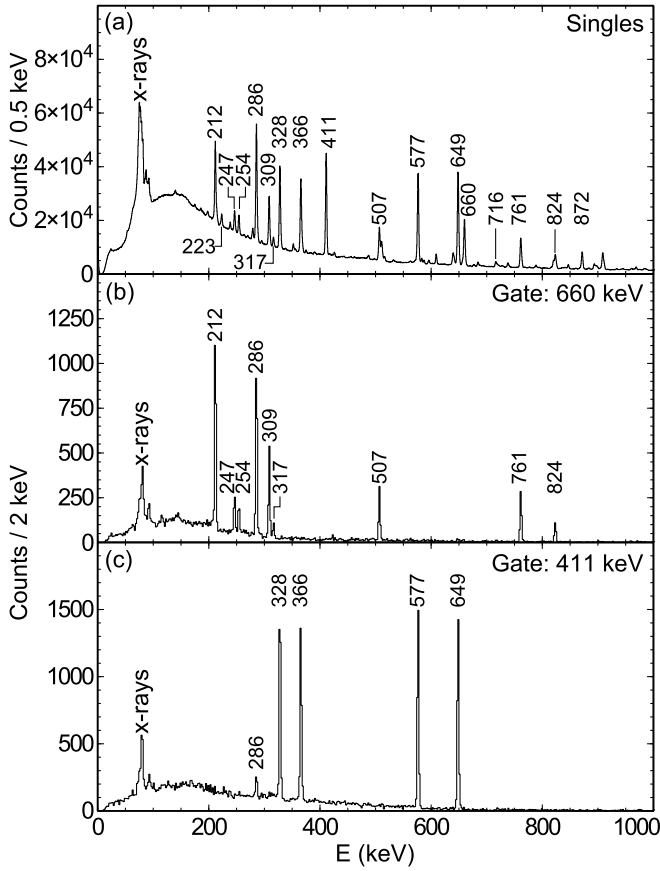


FIG. 3. Energy spectrum of  $\gamma$  rays observed in the focal-plane clover array: (a) Singles, within  $30 \mu\text{s}$  from the recoil implantation. Recoil-gated delayed  $\gamma\gamma$  coincidence energy spectrum when the gating transition is (b) the 660-keV or (c) the 411-keV  $\gamma$ -ray transition.

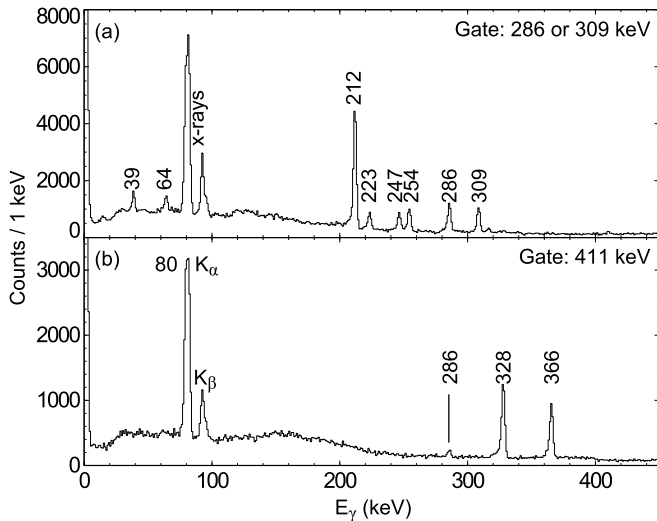


FIG. 4. Energy spectrum of  $\gamma$  rays observed using the planar germanium detector: In the panel (a) a prompt coincidence with the 286 or 309-keV transition observed in the focal-plane clover array is demanded. Panel (b) is the same as the panel (a), but has an energy gate of 411-keV.

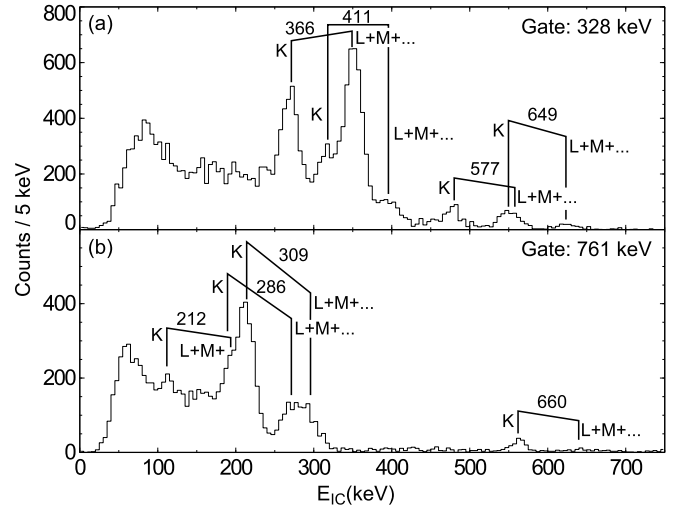


FIG. 5. Energy spectra of internal conversion electrons in prompt coincidence with the 328-keV (a) or 761-keV (b)  $\gamma$ -ray transitions. Conversion electrons are observed in the PIN silicon box array, and the  $\gamma$  rays are observed in the focal-plane clover array.

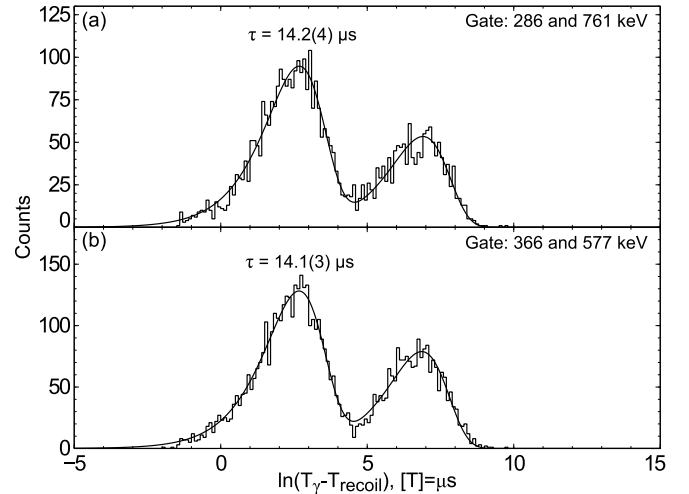


FIG. 6. Natural logarithm of the time difference between the recoil implantation and the subsequent 286-keV (a) or 366-keV (b)  $\gamma$ -ray observation in the planar detector. In addition, the transition observed in the planar detector must be in prompt coincidence with the 761-keV (a) or 577-keV (b)  $\gamma$  ray observed in one of the focal-plane clover detectors. A logarithmic time-scale method [46] yields nearly identical mean lifetime for both distributions. The longer living component is a result of random  $\gamma$ -ray coincidences originating, for example, from Compton scattering. In the extraction of these spectra the  $30 \mu\text{s}$  time gate was omitted.

are a result of reversing start and stop  $\gamma$  rays. After the background subtraction, the centroid  $C$  of each distribution was extracted by using the standard equations [47]

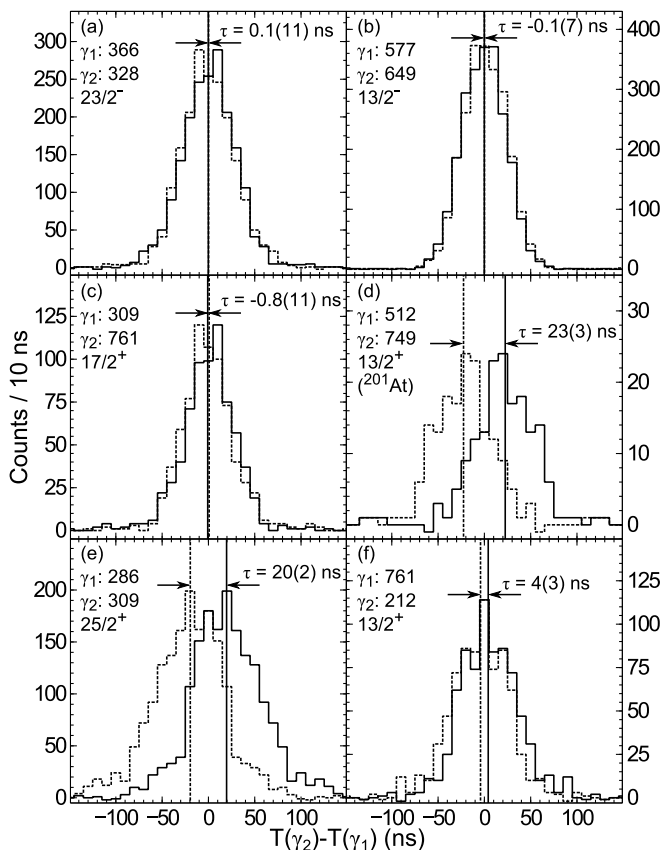


FIG. 7. Time difference between two selected  $\gamma$  rays observed in the focal plane clover array: Panels (a)-(c) show three examples of a prompt time distributions. Panel (d) shows the time difference between 749-keV and 512-keV  $\gamma$  rays in  $^{201}\text{At}$ . This time difference correspond to the mean lifetime of the  $13/2^+$  in  $^{201}\text{At}$ , which has a literature value of 23(2) ns [10]. This time difference was sorted from the data of our earlier experiment, whose results have been published in Refs. [8, 9]. Panels (e) and (f) show the time distributions related to the mean lifetime of the  $25/2^+$  and  $13/2^+$  states in  $^{203}\text{At}$ , respectively. In each panel the dashed distribution is a result of reversing  $\gamma_1$  and  $\gamma_2$  (start and stop). The vertical lines indicate the centroid of each distribution given by Eq. 1 and the given mean lifetimes are extracted through centroid-shift method. The few bins with negative number of counts are due to background subtraction, see text for details.

of

$$C = \frac{\sum_j n_j t_j}{\sum_j n_j} \quad (1)$$

and

$$\delta C = \sqrt{\frac{\sum_j |n_j| (t_j - C)^2}{(\sum_j n_j)^2}}, \quad (2)$$

where  $n_j$  is the number of observations in the time bin  $t_j$ . The absolute value for  $n_j$  in Eq. 2 was added in or-

der to handle a few bins with negative number of events, which are due to background subtraction procedure. Assuming no background contribution after the background subtraction it follows [48] that the centroid shift between normal  $C_N$  and reversed  $C_R$  time distribution is equal to two times the mean lifetime of the state between the start and stop  $\gamma$  ray, hence  $\tau = (C_N - C_R)/2$ . The validity of the method described above was confirmed by extracting the mean lifetime for several states which are assumed to be prompt (Fig. 7(a)-(c)) and also by extracting a mean lifetime of the  $13/2^+$  state in  $^{201}\text{At}$  (Fig. 7(d)). This state is known to have a lifetime of 23(2) ns [10]. The method described above suggests a mean lifetime of 4(3) ns and 20(2) ns for the  $13/2^+$  and  $25/2^+$  states in  $^{203}\text{At}$ , respectively.

## B. Shears band

Figure 8 shows an energy spectrum of prompt  $\gamma$  rays in coincidence with a 949-keV transition. In this spectrum, there are low-energy  $M1$  transitions which, based on  $\gamma\gamma$  coincidences, form a cascade. The  $M1$  assignment is based on a stretched dipole like angular distribution and on a high x-ray yield observed together with this cascade. The  $\gamma$  rays in this cascade are listed in Table II together with the transitions depopulating this band. Table II also lists lower limits for the  $B(M1)/B(E2)$  ratios, which were extracted by integrating the smallest observable peaks in the noise close to the energies of the unobserved  $E2$  overlap transitions. The transition energy of the  $E2$  candidate depopulating the 4639-keV state overlaps with the 544-keV transition, hence it was not possible to integrate the noise close to this energy. Therefore, an average intensity of all the other  $E2$  candidates was used to extract the lower limit of the  $B(M1)/B(E2)$  ratio for the depopulation of this level. This is justified because the noise level through the energy range where the  $E2$  candidates are expected to appear is stable.

There are two observed depopulation paths from the band-head state. A weaker decay path is observed to feed the isomeric  $29/2^+$  state through an 1156-keV stretched dipole transition, see Fig. 9(a). This dipole transition suggests that the band head of the dipole band lies at the excitation energy of 3486 keV with spin of  $27/2$  or  $31/2$ .

The majority of the intensity from the band head state is depopulated through a cascade of 949-keV and 544-keV transitions. Figures 8(a) and (b) show  $\gamma$  rays coinciding with this decay path. Some of these transitions are previously assigned to the positive parity cascade below the isomeric  $29/2^+$  state and those are marked with an asterisk in Figs. 8(a) and (b). The presence of the 309-keV transition suggests that this depopulation path must end up to the  $19/2^+$  state or higher in the positive parity cascade. As the energy of the band-head state is fixed by the 1156-keV transition, energy summing of  $\gamma$  rays suggests that the 949-, 544-keV decay path must populate the

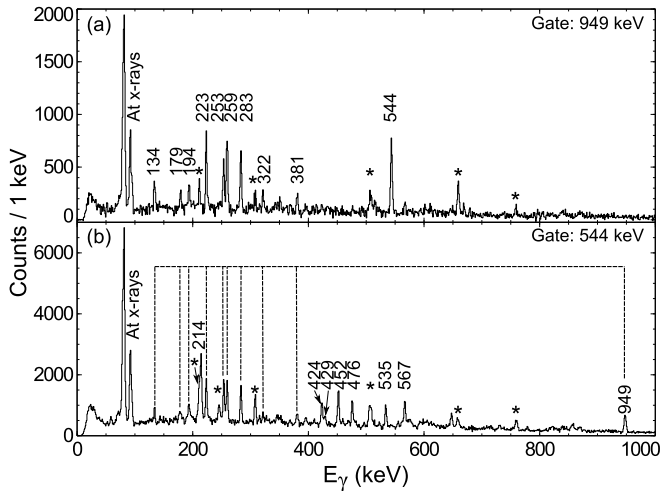


FIG. 8. Energy spectrum of recoil-gated  $\gamma$  rays observed in the JUROGAM II array in coincidence with (a) the 949-keV transition or (b) the 544-keV transition. Transitions labeled with an asterisk are known transitions associated with the positive parity structure below the  $^{29/2^+}$  isomeric state. In panel (b), the dipole band members and the 949-keV transition depopulating the band are connected with a dashed line.

$^{19/2^+}$  state or the  $(^{21/2^+})$  state or both of them. As the 949-keV and 544-keV transitions have a stretched dipole like angular distribution, the spin assignment of  $^{31/2}$  for the band head state can be ruled out. Hence, the spin of the band-head state is likely to be  $(^{27/2^+})$ , which requires the spin of the 1993-keV level to be  $(^{23/2^+})$ . The parity assignment of the dipole band is based on TAC-CDFIT calculations, for more details see Sec. V C. The transition from the 1993-keV  $(^{23/2^+})$  state to the  $(^{21/2^+})$  state would have an  $M1$  character with possible  $E2$  admixture and an energy of 12 keV. Similarly, the transition to the  $^{19/2^+}$  state would be a 51-keV  $E2$  transition. These transition energies were obtained from the energy summing of  $\gamma$ -rays and are both too low to be observed in JUROGAM II. These unobserved transitions are marked with  $\Delta$  and  $\Delta'$  in the level scheme shown in Fig. 2, respectively. Due to these missing transitions the 544-keV and 949-keV transitions are placed tentatively in the level scheme and also the spin and parity assignment for the shears band remain tentative. It is also worth noting that the transitions marked with an asterisk in Fig. 8(a) are lacking some intensity with respect to the 544-keV transition. This might suggest a lifetime of the order of some nanoseconds for the 1993-keV state.

The observed dipole band and depopulation paths are shown in the level scheme in Fig. 2. However, further intensity balance analysis reveals that there must be at least one unobserved decay path from the band head state. Further justification for the shears band assignment is discussed in section V C.

TABLE II. Observed  $\gamma$  rays in the suggested shears band (above the line) and those depopulating the shears structure (below the line). If not specified otherwise,  $E_\gamma$  and  $I_\gamma$  are extracted from the  $\gamma\gamma$  coincidence data gated with the 949-keV transition and  $I_\gamma$  is normalized to the intensity of the 259-keV transition in the recoil gated singles spectrum.

$E_\gamma$ (keV)	$I_\gamma$	$A_2$	$I_i^\pi$	$I_f^\pi$	$B(M1)/B(E2)$ ( $\mu_N^2/e^2b^2$ )
133.8(4)	5.1(10)	<0	$(^{29/2^+})$	$(^{27/2^+})$	-
178.8(5)	3.3(9)	<0	$(^{39/2^+})$	$(^{37/2^+})$	>15
193.6(4)	3.5(6)	<0	$(^{41/2^+})$	$(^{39/2^+})$	>2
223.4(4)	13(3)	<0	$(^{31/2^+})$	$(^{29/2^+})$	>10
253.4(4)	10(2)	<0	$(^{37/2^+})$	$(^{35/2^+})$	>25 <sup>a</sup>
259.4(4)	16(3)	<0	$(^{33/2^+})$	$(^{31/2^+})$	>20
283.3(4)	13(2)	<0	$(^{35/2^+})$	$(^{33/2^+})$	>30
321.7(6)	4.0(11)	<0	$(^{43/2^+})$	$(^{41/2^+})$	>3
381.0(6)	4.4(13)	<0	$(^{45/2^+})$	$(^{43/2^+})$	>5
544.2(5)	26.4(9) <sup>b</sup>	<0	$(^{25/2^+})$	$(^{23/2^+})$	
948.5(7) <sup>b</sup>	8.6(3) <sup>b</sup>	<0	$(^{27/2^+})$	$(^{25/2^+})$	
1155.5(8) <sup>b</sup>	2.24(13) <sup>b</sup>	<0	$(^{27/2^+})$	$^{29/2^+}$	

<sup>a</sup> Extracted using an average  $E2$  intensity of all other  $E2$  candidate transitions. See main text for details.

<sup>b</sup> Extracted from recoil gated singles spectrum

### C. Other observed states

Levels above the isomeric  $^{29/2^+}$  state were probed using the recoil-isomer decay tagging method. Fig. 9(a) shows the singles energy spectrum of prompt  $\gamma$ -rays observed in JUROGAM II by tagging with the depopulation of the  $^{29/2^+}$  state. The used gates are listed in Fig. 9(a), and the  $\gamma$  rays used as a gate were observed in the focal-plane clover array or planar germanium detector. Fig. 9(b) shows an example of recoil-isomer decay tagged  $\gamma\gamma$  coincidence analysis. The observed  $\gamma$ -ray transitions are listed in Table III and those are labeled with group number 1. The level scheme above the isomeric  $^{29/2^+}$  state was constructed based on  $\gamma\gamma$  coincidences, energy sums and intensity balances. Also, the angular distributions of  $\gamma$  rays were extracted when possible. The observed low-energy transitions are not placed in the level scheme due to inconsistencies in the observed transition intensities. However, based on the  $\gamma\gamma$  coincidence data these transitions might form a band-like structure which most likely feeds the 3617-keV state.

The energy of the 1438-keV transition is close to the energy sum of the 920-keV and 520-keV transitions, hence it might be suggested to depopulate the 3770-keV state. This, however, would indicate a spin change of four units assuming that the consecutive 920-keV and 520-keV quadrupole transitions set the spin of the 3770-keV state four units higher with respect to the final  $^{29/2^+}$  state. This would make the 1438-keV transition extremely hindered, hence it is placed tentatively to depopulate a separate state at the energy of 3768 keV.

Also the level scheme of the negative parity cascade was extended significantly. This was done through con-

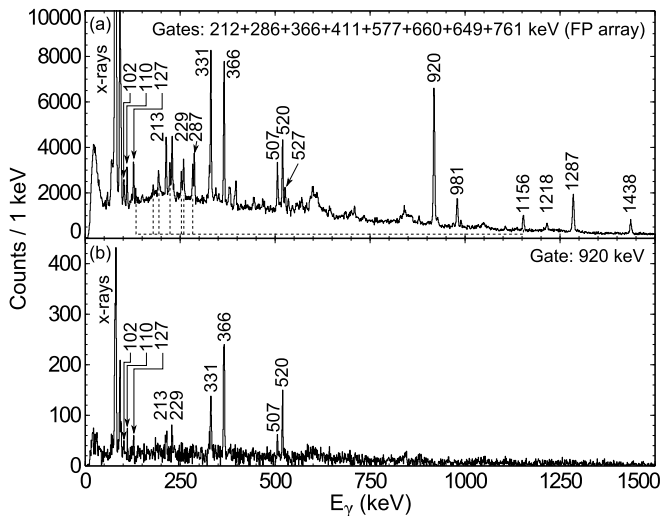


FIG. 9. Recoil-isomer decay tagged prompt  $\gamma$  rays observed in JUROGAMII: (a) Energy spectrum of singles  $\gamma$  rays tagged with any of the most intensive  $\gamma$ -ray transitions depopulating the  $29/2^+$  isomeric state. Transitions connected with a dashed line are associated with the dipole band, see section IV B. (b) An example of recoil-isomer decay tagged  $\gamma\gamma$  coincidence analysis. Energy spectrum of  $\gamma$ -rays in coincidence with the 920-keV  $\gamma$ -transition is shown.

ventional  $\gamma\gamma$  and  $\gamma\gamma\gamma$  coincidence analysis. The observed transitions are listed as group 2 in Table III, and the extended level scheme is presented in Fig. 2.

In addition to the above mentioned transitions, there are seven  $\gamma$ -ray transitions which are only observed to be in coincidence with the 544-keV transition, see Fig. 8(b). These transitions are listed as group 3 in Table III, and those are placed tentatively to the level scheme when possible. Based on the data obtained in this study it was not possible to establish a coincidence between these seven transitions and the rest of the level scheme, other than the 544-keV transition. Therefore, these transitions cannot be firmly assigned to  $^{203}\text{At}$ . However, it is good to bear in mind that Dybdal *et al.* [10] also observed coinciding  $\gamma$  rays with energies of 544.3 keV and 214.8 keV, and based on excitation function study, these were assigned to  $^{203}\text{At}$ .

## V. DISCUSSION

We have performed prompt and delayed spectroscopy for the neutron-deficient nucleus  $^{203}\text{At}$ . The applicable parts of the now extracted level scheme are in good agreement with the level scheme obtained in the earlier study [10]. Also, the presently obtained level scheme for  $^{203}\text{At}$  is remarkably similar compared to the level scheme of  $^{201}\text{At}$  [9]. Therefore, a large fraction of the discussions presented in these earlier studies can be adopted for the low-lying states in  $^{203}\text{At}$ . It is not necessary to repeat these discussions here, but instead the reader is encour-

TABLE III. Other observed  $\gamma$ -ray transitions in  $^{203}\text{At}$ : The  $\gamma$ -ray transitions feeding the  $29/2^+$  isomeric state are listed as group 1.  $E_\gamma$  and  $I_\gamma$  for group 1 transitions are extracted from the recoil-isomer decay tagged JUROGAMII singles data (Fig. 9(a)). Intensities are normalized to the intensity of the 920-keV transition in recoil gated singles spectrum. The  $\gamma$ -ray transitions in the negative parity cascade are listed as group 2.  $E_\gamma$  and  $I_\gamma$  for group 2 transitions are extracted from the 649-keV and 577-keV gated  $\gamma\gamma\gamma$  coincidence data. Intensities are normalized to the intensity of the 411-keV transition in the recoil gated singles spectrum. Transitions in coincidence with the 544-keV transition are listed as group 3.

Group	$E_\gamma$ (keV)	$I_\gamma$	$A_2$	$I_i^\pi$	$I_f^\pi$
1	101.7(4) <sup>a</sup>	1.9(2)			
1	110.1(4) <sup>a</sup>	2.2(2)	<0		
1	127.8(4) <sup>a</sup>	2.1(2)			
1	213.2(4) <sup>a</sup>	2.7(2)			
1	228.9(4) <sup>a</sup>	2.9(2)	>0		
1	287.3(4) <sup>a</sup>	2.2(2)	<0		
1	331.1(4)	8.8(6)	<0		
1	365.8(4)	9.3(6)	>0		
1	506.8(5) <sup>a</sup>	3.8(4)	<0		
1	520.2(5)	5.9(4)	>0	$37/2^+$	$33/2^+$
1	526.9(5) <sup>a</sup>	1.7(3)	<0		
1	919.7(7)	20.7(11)	>0	$33/2^+$	$29/2^+$
1	981.2(7)	4.7(3)	<0		
1	1217.8(8)	1.5(2)			
1	1286.8(8)	8.2(5)			
1	1438.4(9)	2.9(3)	(<0)		
2	265.4(5)	1.6(6)	>0		
2	321.7(5) <sup>a</sup>	4.1(8)	>0		
2	423.3(6)	4.6(14)			
2	430.1(13) <sup>a</sup>	4.3(24)			
2	435.5(6)	9.5(24)	>0	$21/2_2^-$	$21/2_1^-$
2	467.8(8) <sup>a</sup>	1.4(8)			
2	567.9(6)	8.5(15)	>0	$(25/2^-)$	$21/2_2^-$
2	684.1(7)	7.6(15)	>0		
2	709.6(7)	5.5(15)	>0	$(29/2^-)$	$(25/2^-)$
2	847.0(7)	13(2)	>0	$21/2_2^-$	$17/2^-$
2	854.3(7)	11(2)	>0		
2	923.3(7)	2.5(8)			
2	988.5(7)	7.8(14)	<0		
3	214.3(4)	10.8(10)			
3	423.7(5)	5.4(7)	<0		
3	429.0(6) <sup>a</sup>	2.1(5)			
3	452.3(5)	8.5(8)	<0		
3	476.4(5)	5.6(7)			
3	534.5(5)	5.3(8)	>0		
3	567.4(5)	7.9(10)	>0		

<sup>a</sup> Transition not placed in the level scheme

aged to see Refs. [9, 10]. Some of the suggested predominant configurations for the low-lying states are summarized in Table IV. Newly observed states, and those with updated observations are now discussed in more detail.

TABLE IV. Suggested predominant configurations for some of the excited states of  $^{203}\text{At}$ .

E (keV)	$I^\pi$	Configuration	Ref.
649	$13/2^-$	$\pi(h_{9/2}) \otimes  ^{202}\text{Po}; 2^+\rangle$	[9]
660	$11/2^-$	$\pi(h_{9/2}) \otimes  ^{202}\text{Po}; 2^+\rangle$	[9]
872	$13/2^+$	$\pi(i_{13/2}) \otimes \pi(h_{9/2})_{0+}^2$	[10]
1225	$17/2^-$	$\pi(h_{9/2}) \otimes  ^{202}\text{Po}; 4^+\rangle$	[9]
1633	$17/2^+$	$\pi(i_{13/2}) \otimes \pi(h_{9/2})_{2+}^2$	[10]
1636	$21/2^-$	$\pi(h_{9/2}) \otimes  ^{202}\text{Po}; 6^+\rangle$	[9]
1696	$17/2^+$	$\pi(h_{9/2}) \otimes  ^{202}\text{Po}; 5^-\rangle$	[10]
1942	$19/2^+$	$\pi(h_{9/2}) \otimes  ^{202}\text{Po}; 5^-\rangle$	[10]
1964	$23/2^-$	$\pi(f_{7/2}) \otimes  ^{202}\text{Po}; 8^+\rangle$	
1981	$21/2^+$	$\pi(h_{9/2}) \otimes  ^{202}\text{Po}; 7^-\rangle$	
2045	$25/2^+$	$\pi(h_{9/2}) \otimes  ^{202}\text{Po}; 9^-\rangle$	
2330	$29/2^+$	$\pi(h_{9/2}) \otimes  ^{202}\text{Po}; 11^-\rangle$	
3250	$33/2^+$	$ \pi(h_{9/2}^2 i_{13/2}); 29/2^+\rangle \otimes  ^{200}\text{Pb}; 2^+\rangle$	
3770	$37/2^+$	$ \pi(h_{9/2}^2 i_{13/2}); 29/2^+\rangle \otimes  ^{200}\text{Pb}; 4^+\rangle$	

### A. Isomeric $^{29/2^+}$ state

Figure 10(a) shows the systematics of the  $^{29/2^+}$ ,  $^{25/2^+}$  and  $^{23/2^-}$  states in astatine nuclei. These states are compared to the  $11^-$  [ $\pi(h_{9/2} i_{13/2})$ ],  $9^-$  [ $\nu(f_{5/2}^{-1} i_{13/2}^{-1})$ ] and  $8^+$  [ $\pi(h_{9/2}^2)$ ] states observed in respective polonium isotones. In Fig 10(a) it is evident that the isomeric  $^{29/2^+}$  state in astatine isotopes appear to follow the isomeric  $11^-$  state in polonium isotopes. Moreover, the astatine states  $^{25/2^+}$  and  $^{23/2^-}$  appear to follow the systematic trends of the  $9^-$  and  $8^+$  states observed in polonium nuclei, respectively. In polonium nuclei, it has been observed [49, 50] that the isomeric  $11^-$  state can be depopulated to  $9^-$  and  $8^+$  states through  $E2$  and  $E3$  transitions, respectively. Based on the above mentioned systematic trends one may propose that the now observed  $^{29/2^+}$  and  $^{25/2^+}$  states in astatine nuclei are a result of a coupling of the odd  $h_{9/2}$  proton to the  $11^-$  or  $9^-$  states of the polonium core, respectively. Similarly, the  $^{23/2^-}$  state can be suggested to originate from the odd  $f_{7/2}$  proton coupled to the  $8^+$  state of the polonium core. These interpretations are identical to those suggested earlier for the applicable states in astatine isotopes  $^{199,201,205,209,211}\text{At}$  [7, 9, 11, 13, 14].

The observed mean lifetime of  $14.1(3) \mu\text{s}$  corresponds to reduced transition strengths of  $21(2) \text{ W.u.}$  and  $1.92(14) \cdot 10^{-4} \text{ W.u.}$  for the  $E3$  and  $E2$  transitions depopulating the isomeric  $^{29/2^+}$  state in  $^{203}\text{At}$ , respectively. The observed strong hindrance for the  $E2$  transition is understandable as this transition involves a significant structural difference between the initial and final states. Unlike the  $E2$  transition, the  $E3$  transition is strongly favored. This is a fairly common feature of the  $E3$  transitions observed in nuclei above lead. It is understood as a

coupling of a particle configuration to the octupole vibrations of the core, which gives a collective component for the  $E3$  transition [51]. In Fig 10(b), the above mentioned transition strengths are compared to the analogous values in neighboring astatine isotopes. From Fig. 10(b), one may observe that the  $B(E3)$  value stays roughly constant in all of the astatine isotopes, however, starting from  $^{201}\text{At}$  ( $N=116$ ) there is a rapid increase in the  $B(E2)$  value. This, together with the energy systematics, explains the observed intensity balance between the  $E2$  and  $E3$  transitions in different astatine isotopes. In  $^{199}\text{At}$ , only the  $E2$  transition is observed. In  $^{201}\text{At}$ , both transitions are observed but the  $E2$  dominates. In  $^{203}\text{At}$ , both transitions are observed with comparable intensities. In  $^{205}\text{At}$ , again both transitions are observed but this time the  $E3$  transition dominates and finally, in  $^{209,211}\text{At}$  only the  $E3$  transition is observed.

It is also worth mentioning that there are recent observations [52, 53] of a similar  $^{29/2^+}$  isomeric state in the nearby nuclei  $^{193,195}\text{Bi}$ . In bismuth nuclei, the isomeric state has been suggested to originate from the same  $\pi(i_{13/2} h_{9/2}^2)$  coupling. However, this requires an excitation of a proton pair across the  $Z = 82$  shell closure, which explains the higher excitation energy of the  $^{29/2^+}$  isomer in Bi nuclei. For further details of the  $^{29/2^+}$  isomeric state in bismuth nuclei, see Refs. [52, 53].

### B. States above the isomeric $^{29/2^+}$ state

As discussed above, the isomeric  $^{29/2^+}$  state in astatine is interpreted to originate from the  $i_{13/2}$  proton coupled to a fully-aligned  $h_{9/2}$  proton pair. Therefore, achieving an angular momentum higher than  $^{29/2}$  must involve a structural change with respect to the configuration of the isomeric  $^{29/2^+}$  state. One option is to couple the  $i_{13/2} h_{9/2}^2$  proton configuration to a low-lying neutron state of the respective polonium core. In nearby polonium isotopes the lowest known neutron states are  $5^-$  and  $7^-$  [59], both originating mainly from the  $\nu i_{13/2} p_{3/2}^{-1}$  configuration. Another way to increase the angular momentum beyond  $^{29/2^+}$  is to couple this state to a low-lying state of the respective Pb core. This was also suggested in our earlier publication [9] for  $^{201}\text{At}$ , but the discussion presented there was very limited.

In Fig. 11 the energies of the  $^{33/2^+}$  and  $^{37/2^+}$  states feeding the isomeric  $^{29/2^+}$  state are shown together with a low-lying  $2^+$  and  $4^+$  states of the respective Pb core. Figure 11 also shows the energies of the  $5^-$  and  $7^-$  neutron states observed in polonium nuclei. From the figure, one may observe that the energy spacing of the  $^{33/2^+}$  and  $^{37/2^+}$  states in astatine is similar to the energy spacing of the  $2^+$  and  $4^+$  states in Pb nuclei. Therefore, one may suggest that the  $^{33/2^+}$  and  $^{37/2^+}$  states in astatine nuclei originate from the coupling of the  $i_{13/2} h_{9/2}^2$  proton configuration to the  $2^+$  and  $4^+$  states of the Pb core.

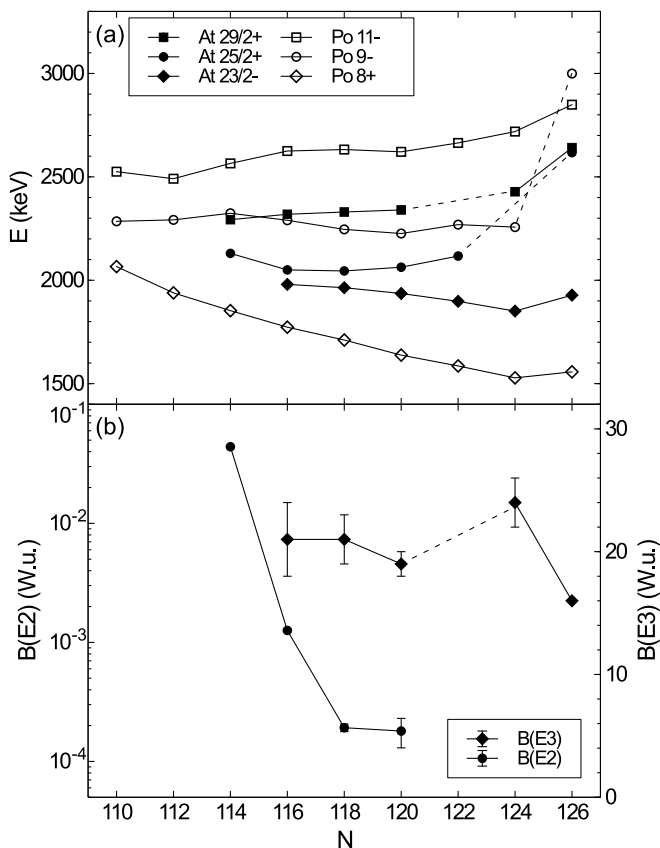


FIG. 10. Panel (a) shows the energy systematics of the isomeric  $29/2^+$  and the subsequent  $25/2^+$  and  $23/2^-$  states in astatine isotopes (solid symbols). These states are compared to the systematics of the analogous isomeric  $11^-$  states in polonium isotopes (open symbols). In panel (b) the reduced transition strengths for the transitions depopulating the isomeric  $29/2^+$  state are shown. Note the scales in panel (b). Data for At isotopes are taken from Refs [7, 9, 11–14, 54] and this work and for Po isotopes from Refs. [4, 50, 55–58]. Neutron number of  $^{203}\text{At}$  is 118.

### C. Shears band

Shears bands have certain characteristic properties which may be summarized as follows [16]:

1. The level energies in the band (away from band crossings) follow the pattern of  $E(I) - E_0 \propto (I - I_0)^2$ , where 0 refers to the band head state.
2. The band is formed from strong  $M1$  transitions with possible weak  $E2$  crossovers. Usually  $B(M1)/B(E2) \gtrsim 20 \mu_N^2/e^2b^2$ , and  $B(M1) \sim 2 - 10 \mu_N^2$ .
3. The nucleus has a small quadrupole deformation.
4. The active orbitals must involve high  $j$  values.
5. The ratio of the dynamic moment of inertia over  $B(E2)$  is large,  $>100 \text{ MeV}^{-1}(\text{eb})^{-2}$ , when com-

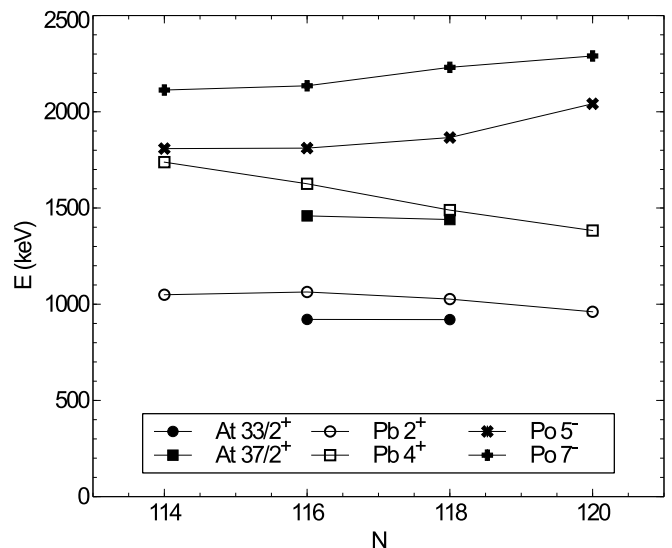


FIG. 11. Energy systematics of the states above the isomeric  $29/2^+$  state normalized to the energy of the  $29/2^+$  state in  $^{201,203}\text{At}$  (solid symbols). These energies are compared to the energies of the  $2^+$  and  $4^+$  states in the nearby lead nuclei. For comparison, also the two lowest lying neutron states known in polonium nuclei are shown. Energies for the states in Pb nuclei are taken from Refs. [60–63], for Po from Refs. [49, 59, 64] and for At this work and Ref. [9]. Neutron numbers of  $^{201,203}\text{At}$  are 116 and 118, respectively.

pared to well-deformed ( $\sim 10 \text{ MeV}^{-1}(\text{eb})^{-2}$ ) or superdeformed ( $\sim 5 \text{ MeV}^{-1}(\text{eb})^{-2}$ ) bands.

The above listed properties are now compared to the properties of the dipole band observed in  $^{203}\text{At}$ .

Figure 12 shows the energy of the levels in the observed band as a function of the level spin. The dashed lines in Fig. 12 represents two parabolas fitted independently to the low- and high-spin part of the band. As one may observe, the energies of the cascade are well reproduced by these two parabolas, hence, the characteristic property number 1, listed above, is satisfied with one band crossing taking place at spin and excitation energy of  $\sim 18 \hbar$  and  $\sim 4.6 \text{ MeV}$ , respectively. This band crossing can also be seen as a backbending in the inset of Fig. 12.

As discussed in Section IV B, the high x-ray yield and the angular distribution of  $\gamma$  rays suggest an  $M1$  character for the transitions in the  $^{203}\text{At}$  band. Moreover, the lack of  $E2$  crossover transitions and the extracted lower limit for the  $B(M1)/B(E2)$  values listed in Table II suggest that the observed dipole cascade in  $^{203}\text{At}$  satisfies the characteristic property number 2 listed above. However, it was not possible to extract the exact  $B(M1)$  or  $B(E2)$  values from our data.

Total Routhian Surface calculations, presented in Ref. [65], predict a small prolate deformation for the ground state of  $^{203}\text{At}$ . As there is no observation of a rotational-like level pattern in  $^{203}\text{At}$  it can be suggested that the ground state of  $^{203}\text{At}$  is nearly spherical. This idea is supported by the fact that the  $^{202}\text{Po}$  core nucleus is known

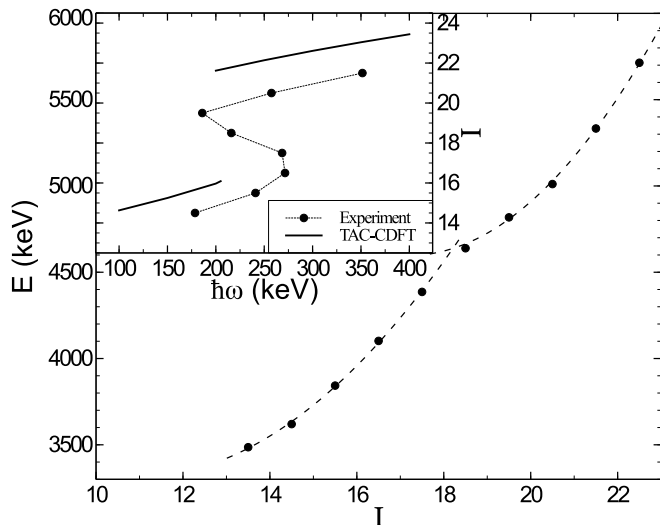


FIG. 12. Energy of the levels in the dipole band as a function of spin. The dashed lines are two independent parabolas fitted to the low- and high-spin part of the cascade to guide the eye. The inset shows the spin of the shears band as a function of rotational frequency. This is compared to the covariant density functional (TAC-CDFT) calculations (solid line) for  $\pi(i_{13/2}) \otimes \nu(i_{13/2})$  and  $\pi(h_{9/2}^2 i_{13/2}) \otimes \nu(i_{13/2})$  configurations below and above the band crossing, respectively.

to be nearly spherical based on an in-source resonant ionization laser spectroscopy study [66] and Coulomb-excitation study [67]. A near spherical shape is required for the observation of a shears band because in well deformed nuclei the core rotation dominates over the shears mechanism (characteristic property No. 3).

The configuration assignment for the shears band was done through TAC-CDFT calculations as described in Sec. III. These calculations suggest a configuration of  $\pi(i_{13/2}) \otimes \nu(i_{13/2})$  and  $\pi(h_{9/2}^2 i_{13/2}) \otimes \nu(i_{13/2})$  below and above the band crossing, respectively. These configurations suggest a positive parity for the dipole band. A comparison between angular momenta of the now observed dipole band and the results of the TAC-CDFT calculations are presented in the inset of Fig 12. It is worth noting that the TAC-CDFT can not produce converged results in the backbending region because such a phenomenon is beyond the scope of the cranking calculation [68]. Furthermore, it is found through TAC-CDFT that, for the configuration of  $\pi(i_{13/2}) \otimes \nu(i_{13/2})^{-2}$ , the proton quasi-particle in the  $i_{13/2}$  orbital contributes with an angular momentum of about  $6.4\hbar$  and the two quasi-neutrons in the same orbital generate an angular momentum of  $\sim 11.5\hbar$ . The appearance of the backbending is due to the alignment of the two  $h_{9/2}$  quasi-protons, which provide an extra angular momentum of about  $7 \sim 8\hbar$ . In the present calculations, the shears mechanism has been found for both configurations by checking the angular momentum decomposition. Moreover, the  $i_{13/2}$  and  $h_{9/2}$  proton orbitals as well as the  $i_{13/2}$  neutron orbital, can be considered as high- $j$  orbitals, hence, the observed dipole

TABLE V. Reduced transition strengths for the transitions depopulating the  $^{13/2^+}$  state in  $^{201,203}\text{At}$  and the  $^{25/2^+}$  state in  $^{203}\text{At}$ . The data for  $^{201}\text{At}$  was obtained by using a mean lifetime of 23(2) ns [10] for the  $^{13/2^+}$  state and a level structure reported in Ref. [9].

$B(\sigma\lambda; I_i^\pi \rightarrow I_f^\pi)$	$^{201}\text{At}$ (W.u.)	$^{203}\text{At}$ (W.u.)
$B(M2; ^{13/2^+} \rightarrow 9/2^-)$	0.18(4)	0.22(14)
$B(E1; ^{13/2^+} \rightarrow ^{13/2^-})$	$6.2(13) \cdot 10^{-7}$	$4(3) \cdot 10^{-7}$
$B(E1; ^{13/2^+} \rightarrow ^{11/2^-})$	$2.2(9) \cdot 10^{-6}$	$4(3) \cdot 10^{-6}$
$B(E2; ^{25/2^+} \rightarrow ^{21/2^+})$		8.2(7)
$B(E1; ^{25/2^+} \rightarrow ^{23/2^-})$		$1.1(4) \cdot 10^{-6}$

band satisfies the characteristic property number 4.

As there is no lifetime data available for the dipole band states it is not possible to extract the exact  $B(M1)$  or  $B(E2)$  values, hence the property No. 5 can not be addressed here. However, as discussed above the observed dipole band appears to satisfy the listed characteristic properties 1-4 of shears bands. Therefore, the now observed dipole band can be suggested to originate from the shears mechanism.

#### D. Isomeric $^{13/2^+}$ and $^{25/2^+}$ states

It is worth expanding this discussion also to the isomeric  $^{13/2^+}$  and  $^{25/2^+}$  states, even though these states are present in the level scheme of the previous study [10]. In this study, the level structure around the  $^{25/2^+}$  state was clarified and a lifetime was extracted for both of the mentioned states. The reduced transition strengths corresponding to the extracted lifetimes are shown in the Table V. As the depopulation of the  $^{13/2^+}$  state in  $^{201}\text{At}$  state was updated recently [9], also the reduced transition strengths for the transitions depopulating this state are revised. This was done by using the mean lifetime of 23(2) ns [10] and the recent [9] data for the depopulation of the state. These results are also reported in Table V. In Fig. 13 these transition strengths are compared to the strengths of the respective transitions in neighboring astatine nuclei. From the figure one may observe that the obtained transition strength values are in good agreement with the values reported earlier for the same transitions in nearby astatine nuclei. The  $B(M2)$  values of 0.18(4) and 0.22(14) W.u. for the  $^{13/2^+} \rightarrow 9/2^-$  transition in  $^{201,203}\text{At}$ , respectively, are comparable to the values of 0.10(2) W.u. [69] and 0.17(4) W.u. [70] obtained for the same transition in nearby francium nuclei  $^{203,205}\text{Fr}$ , respectively. In francium nuclei the  $^{13/2^+}$  state is also suggested to originate from the  $\pi(i_{13/2})$  configuration.

The  $E2$  transition depopulating the  $^{25/2^+}$  state is enhanced. The initial and final state configurations for the mentioned  $E2$  transition are  $\pi(h_{9/2}) \otimes |^{202}\text{Po}; 9^- \rangle$  and  $\pi(h_{9/2}) \otimes |^{202}\text{Po}; 7^- \rangle$ , respectively. The dominant component of the polonium state wave functions are  $\nu i_{13/2}^{-1} f_{5/2}^{-1}$

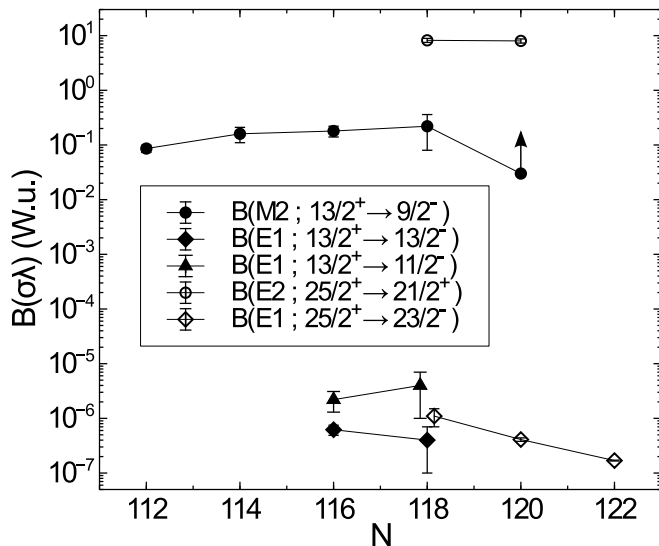


FIG. 13. Reduced transition strengths for the transitions depopulating the  $13/2^+$  (solid symbols) and  $25/2^+$  (open symbols) isomeric states in astatine nuclei. The data point with an arrow is to be considered as a lower limit. Data for this plot was obtained from the Refs. [7, 11, 65] and the present work. Some of the  $^{203}\text{At}$  data points ( $N=118$ ) are shifted slightly horizontally for better visualization.

and  $\nu i_{13/2}^{-1} p_{3/2}^{-1}$ , respectively, but the wave function of the  $7^-$  state also has a  $\nu i_{13/2}^{-1} f_{5/2}^{-1}$  component [59]. This gives a collective component for the  $25/2^+ \rightarrow 21/2^+$   $E2$  transition which agrees well with the observed enhanced transition strength.

The extracted  $B(E1)$  values for the three  $E1$  transitions suggest a strong hindrance of the order of  $10^6$  or  $10^7$  W.u. For each  $E1$  transition, the configuration of the initial and final states are remarkably different. In such a case, the reduced transition strengths of  $10^{-6}$  or  $10^{-7}$  W.u for  $E1$  transitions in the lead region are common.

## VI. SUMMARY

We have performed prompt and delayed spectroscopy of the neutron deficient nucleus  $^{203}\text{At}$ . We have observed

an isomeric state with a spin and parity of  $29/2^+$ . The isomeric state has a mean lifetime of  $14.1(3) \mu\text{s}$ , which corresponds to reduced transition strengths of  $21(2)$  W.u. and  $1.92(14) \cdot 10^{-4}$  W.u. for the deexciting 366-keV  $E3$  and 286-keV  $E2$  transitions, respectively. The isomeric state is suggested to originate from the  $\pi(h_{9/2}) \otimes |^{202}\text{Po}; 11^- \rangle$  configuration. The states above the isomeric  $29/2^+$  state in odd-mass astatine isotopes exhibits similar systematic trends as do the low-lying states in lead nuclei. In addition, the observed properties of a new dipole band satisfy the characteristic properties of a shears band, hence it is suggested to arise from the shears mechanism.

## VII. ACKNOWLEDGMENTS

The authors thank P. W. Zhao for helpful discussions and careful reading of the manuscript. This work has been supported by the Academy of Finland under the Finnish Center of Excellence Programme (Contract number 213503). The authors also thank the GAMMAPOOL European Spectroscopy Resource for the loan of the detectors for the JUROGAM II array. Support has also been provided by the EU 7th framework programme, Project No. 262010 (ENSAR). KA acknowledges that this material is partially based upon work supported by the U.S Department of Energy, Office of Science, Office of Nuclear Physics, under contract number DE-AC02-06CH11357. AH and MJM acknowledges a partial support by the United Kingdom Science and Technology Facilities Council (STFC). YKW acknowledges that this work is partially supported by the Major State 973 Program of China (Grant No. 2013CB834400), the National Natural Science Foundation of China (Grants No. 11335002, No. 11375015, No. 11461141002, No. 11621131001).

- 
- [1] K. Heyde, P. V. Isacker, M. Waroquier, J. Wood, and R. Meyer, Phys. Rep. **102**, 291 (1983).  
 [2] J. Wood, K. Heyde, W. Nazarewicz, M. Huyse, and P. van Duppen, Phys. Rep. **215**, 101 (1992).  
 [3] R. Julin, K. Helariutta, and M. Muikku, J. Phys. G **27**, R109 (2001).  
 [4] K. Helariutta, J. Cocks, T. Enqvist, P. Greenlees, P. Jones, R. Julin, S. Juutinen, P. Jämsen, H. Kankaanpää, H. Kettunen, P. Kuusiniemi, M. Leino, M. Muikku, M. Piiparinen, P. Rahkila, A. Savelius, W. Trzaska, S. Törmänen, J. Uusitalo, R. Allatt, P. Butler, R. Page, and M. Kapusta, Eur. Phys. J. A **6**, 289 (1999).  
 [5] K. Van de Vel, A. Andreyev, R. Page, H. Kettunen, P. Greenlees, P. Jones, R. Julin, S. Juutinen, H. Kankaanpää, A. Keenan, P. Kuusiniemi, M. Leino, M. Muikku, P. Nieminen, P. Rahkila, J. Uusitalo, K. Eskola, A. Hrstel, M. Huyse, Y. L. Coz, M. Smith, P. V. Duppen, and R. Wyss, Eur. Phys. J. A **17**, 167 (2003).  
 [6] M. Nyman, S. Juutinen, I. Darby, S. Eeckhaudt, T. Grahn, P. Greenlees, U. Jakobsson, P. Jones, R. Julin, S. Ketelhut, H. Kettunen, M. Leino, P. Nieminen,

- P. Peura, P. Rahkila, J. Sarén, C. Scholey, J. Sorri, J. Uusitalo, and T. Enqvist, *Phys. Rev. C* **88**, 054320 (2013).
- [7] U. Jakobsson, J. Uusitalo, S. Juutinen, M. Leino, P. Nieminen, K. Andgren, B. Cederwall, P. Greenlees, B. Hadinia, P. Jones, R. Julin, S. Ketelhut, A. Khaplanov, M. Nyman, P. Peura, P. Rahkila, P. Ruotsalainen, M. Sandzelius, J. Sarén, C. Scholey, and J. Sorri, *Phys. Rev. C* **82**, 044302 (2010).
- [8] K. Auranen, J. Uusitalo, S. Juutinen, U. Jakobsson, T. Grahn, P. T. Greenlees, K. Hauschild, A. Herzán, R. Julin, J. Konki, M. Leino, J. Pakarinen, J. Partanen, P. Peura, P. Rahkila, P. Ruotsalainen, M. Sandzelius, J. Sarén, C. Scholey, J. Sorri, and S. Stolze, *Phys. Rev. C* **90**, 024310 (2014).
- [9] K. Auranen, J. Uusitalo, S. Juutinen, U. Jakobsson, T. Grahn, P. T. Greenlees, K. Hauschild, A. Herzán, R. Julin, J. Konki, M. Leino, J. Pakarinen, J. Partanen, P. Peura, P. Rahkila, P. Ruotsalainen, M. Sandzelius, J. Sarén, C. Scholey, J. Sorri, and S. Stolze, *Phys. Rev. C* **91**, 024324 (2015).
- [10] K. Dybdal, T. Chapuran, D. Fossan, W. Piel, D. Horn, and E. Warburton, *Phys. Rev. C* **28**, 1171 (1983).
- [11] R. Davie, A. Poletti, G. Dracoulis, A. Byrne, and C. Fahlander, *Nucl. Phys. A* **430**, 454 (1984).
- [12] T. P. Sjoreen, U. Garg, and D. B. Fossan, *Phys. Rev. C* **23**, 272 (1981).
- [13] T. Sjoreen, G. Schatz, S. Bhattacharjee, B. Brown, D. Fossan, and P. Lesser, *Phys. Rev. C* **14**, 1023 (1976).
- [14] I. Bergström, B. Fant, C. J. Herrlander, K. Wikström, and J. Blomqvist, *Phys. Scr.* **1**, 243 (1970).
- [15] D. J. Hartley, E. P. Seyfried, W. Reviol, D. G. Sarantites, C. J. Chiara, O. L. Pechenaya, K. Hauschild, A. Lopez-Martens, M. P. Carpenter, R. V. F. Janssens, D. Seweryniak, and S. Zhu, *Phys. Rev. C* **78**, 054319 (2008).
- [16] R. M. Clark and A. O. Macchiavelli, *Annu. Rev. Nucl. Part. Sci.* **50**, 1 (2000).
- [17] A. Gadea, G. de Angelis, C. Fahlander, M. De Poli, E. Farnea, Y. Li, D. Napoli, Q. Pan, P. Spolaore, D. Bazzacco, S. Lenzi, S. Lunardi, C. Petrache, F. Brandolini, P. Pavan, C. Rossi Alvarez, M. Sferrazza, P. Bizzeti, A. Bizzeti Sona, J. Nyberg, M. Lipoglavsek, J. Persson, J. Cederkäll, D. Seweryniak, A. Johnson, H. Grawe, F. Soramel, M. Ogawa, A. Makishima, R. Schubart, and S. Frauendorf, *Phys. Rev. C* **55**, R1 (1997).
- [18] D. Jenkins, I. Hibbert, C. Parry, R. Wadsworth, D. Fossan, G. Lane, J. Sears, J. Smith, R. Clark, R. Krcken, I. Lee, A. Macchiavelli, V. Janzen, J. Cameron, and S. Frauendorf, *Phys. Lett. B* **428**, 23 (1998).
- [19] R. Clark, S. Asztalos, B. Busse, C. Chiara, M. Cromaz, M. Deleplanque, R. Diamond, P. Fallon, D. Fossan, D. Jenkins, S. Juutinen, N. Kelsall, R. Krücken, G. Lane, I. Lee, A. Macchiavelli, R. MacLeod, G. Schmid, J. Sears, J. Smith, F. Stephens, K. Vetter, R. Wadsworth, and S. Frauendorf, *Phys. Rev. Lett.* **82**, 3220 (1999).
- [20] F. Brandolini, M. Ionescu-Bujor, N. Medina, R. Ribas, D. Bazzacco, M. D. Poli, P. Pavan, C. R. Alvarez, G. de Angelis, S. Lunardi, D. D. Acua, D. Napoli, and S. Frauendorf, *Phys. Lett. B* **388**, 468 (1996).
- [21] J. R. Novak, C. W. Beausang, N. Amzal, R. F. Casten, G. Cata Danil, J. F. C. Cocks, J. R. Cooper, P. T. Greenlees, F. Hannachi, K. Helariutta, P. Jones, R. Julin, S. Juutinen, H. Kankaanpää, H. Kettunen, R. Krücken, P. Kuusiniemi, M. Leino, B. Liu, M. Muikku, A. Savelius, T. Socci, J. T. Thomas, N. V. Zamfir, J.-y. Zhang, and S. Frauendorf, *Phys. Rev. C* **59**, R2989 (1999).
- [22] S. Frauendorf, *Nucl. Phys. A* **557**, 259 (1993).
- [23] P. Zhao, S. Zhang, J. Peng, H. Liang, P. Ring, and J. Meng, *Physics Letters B* **699**, 181 (2011).
- [24] J. Meng, J. Peng, S.-Q. Zhang, and P.-W. Zhao, *Frontiers of Physics* **8**, 55 (2013).
- [25] J. Meng and P. Zhao, *Physica Scripta* **91**, 053008 (2016).
- [26] L. F. Yu, P. W. Zhao, S. Q. Zhang, P. Ring, and J. Meng, *Phys. Rev. C* **85**, 024318 (2012).
- [27] P. W. Zhao, J. Peng, H. Z. Liang, P. Ring, and J. Meng, *Phys. Rev. Lett.* **107**, 122501 (2011).
- [28] P. W. Zhao, J. Peng, H. Z. Liang, P. Ring, and J. Meng, *Phys. Rev. C* **85**, 054310 (2012).
- [29] P. Zhao, *Physics Letters B* **773**, 1 (2017).
- [30] P. W. Zhao, N. Itagaki, and J. Meng, *Phys. Rev. Lett.* **115**, 022501 (2015).
- [31] P. W. Zhao, S. Q. Zhang, and J. Meng, *Phys. Rev. C* **92**, 034319 (2015).
- [32] G. Duchne, F. Beck, P. Twin, G. de France, D. Curien, L. Han, C. Beausang, M. Bentley, P. Nolan, and J. Simpson, *Nucl. Instrum. Methods Phys. Res., Sect. A* **432**, 90 (1999).
- [33] C. Beausang, S. Forbes, P. Fallon, P. Nolan, P. Twin, J. Mo, J. Lisle, M. Bentley, J. Simpson, F. Beck, D. Curien, G. deFrance, G. Duchne, and D. Popescu, *Nucl. Instrum. Methods Phys. Res., Sect. A* **313**, 37 (1992).
- [34] C. R. Alvarez, *Nucl. Phys. News* **3**, 10 (1993).
- [35] E. D. Mateosian and A. Sunyar, *At. Data and Nucl. Data Tables* **13**, 391 (1974).
- [36] M. Leino, J. Äystö, T. Enqvist, P. Heikkinen, A. Jokinen, M. Nurmia, A. Ostrowski, W. Trzaska, J. Uusitalo, K. Eskola, P. Armbruster, and V. Ninov, *Nucl. Instr. Methods Phys. Res., Sect. B* **99**, 653 (1995).
- [37] J. Sarén, J. Uusitalo, M. Leino, and J. Sorri, *Nucl. Instr. Methods Phys. Res., Sect. A* **654**, 508 (2011).
- [38] R. Page, A. Andreyev, D. Appelbe, P. Butler, S. Freeman, P. Greenlees, R.-D. Herzberg, D. Jenkins, G. Jones, P. Jones, D. Joss, R. Julin, H. Kettunen, M. Leino, P. Rahkila, P. Regan, J. Simpson, J. Uusitalo, S. Vincent, and R. Wadsworth, *Nucl. Instrum. Methods Phys. Res., Sect. B* **204**, 634 (2003).
- [39] I. Lazarus, D. Appelbe, P. Butler, P. Coleman-Smith, J. Cresswell, S. Freeman, R. Herzberg, I. Hibbert, D. Joss, S. Letts, R. Page, V. Pucknell, P. Regan, J. Sampson, J. Simpson, J. Thornhill, and R. Wadsworth, *IEEE Trans. Nucl. Sci.* **48**, 567 (2001).
- [40] P. Rahkila, *Nucl. Instrum. Methods Phys. Res., Sect. A* **595**, 637 (2008).
- [41] Y. K. Wang, *Phys. Rev. C* **96**, 054324 (2017).
- [42] Y. Tian, Z. Ma, and P. Ring, *Physics Letters B* **676**, 44 (2009).
- [43] P. W. Zhao, Z. P. Li, J. M. Yao, and J. Meng, *Phys. Rev. C* **82**, 054319 (2010).
- [44] T. Kibédi, T. Burrows, M. Trzhaskovskaya, P. Davidson, and C. N. Jr., *Nucl. Instrum. Methods Phys. Res., Sect. A* **589**, 202 (2008).
- [45] K. Auranen, J. Uusitalo, S. Juutinen, H. Badran, F. D. Bisso, D. Cox, T. Grahn, P. T. Greenlees, A. Herzán, U. Jakobsson, R. Julin, J. Konki, M. Leino, A. Lightfoot, M. Mallaburn, O. Neuvonen, J. Pakarinen, P. Papadakis, J. Partanen, P. Rahkila, M. Sandzelius, J. Sarén, C. Sc-

- holey, J. Sorri, and S. Stolze, *Phys. Rev. C* **95**, 044311 (2017).
- [46] K. Schmidt, *The European Physical Journal A* **8**, 141 (2000).
- [47] H. Mach, R. Gill, and M. Moszyński, *Nuclear Instruments and Methods in Physics Research Section A: Accelerators, Spectrometers, Detectors and Associated Equipment* **280**, 49 (1989).
- [48] J.-M. Régis, G. Pascovici, J. Jolie, and M. Rudigier, *Nuclear Instruments and Methods in Physics Research Section A: Accelerators, Spectrometers, Detectors and Associated Equipment* **622**, 83 (2010).
- [49] A. Maj, H. Grawe, H. Kluge, A. Kuhnert, K. Maier, J. Recht, N. Roy, H. Hbel, and M. Guttormsen, *Nucl. Phys. A* **509**, 413 (1990).
- [50] H. Beuscher, D. R. Zolnowski, D. R. Haenni, and T. T. Sugihara, *Phys. Rev. Lett.* **36**, 1128 (1976).
- [51] I. Bergström and B. Fant, *Phys. Scr.* **31**, 26 (1985).
- [52] A. Herzáň, S. Juutinen, K. Auranen, T. Grahn, P. T. Greenlees, K. Hauschild, U. Jakobsson, P. Jones, R. Julin, S. Ketelhut, M. Leino, A. Lopez-Martens, P. Nieminen, M. Nyman, P. Peura, P. Rahkila, S. Rinta-Antila, P. Ruotsalainen, M. Sandzelius, J. Sarén, C. Scholey, J. Sorri, and J. Uusitalo, *Phys. Rev. C* **92**, 044310 (2015).
- [53] A. Herzáň, S. Juutinen, K. Auranen, T. Grahn, P. T. Greenlees, K. Hauschild, U. Jakobsson, R. Julin, S. Ketelhut, M. Leino, A. Lopez-Martens, T. Lönnroth, P. Nieminen, M. Nyman, J. Partanen, P. Peura, P. Rahkila, P. Ruotsalainen, M. Sandzelius, J. Sarén, C. Scholey, J. M. K. Slotte, J. Sorri, S. Stolze, and J. Uusitalo, *Phys. Rev. C* **96**, 014301 (2017).
- [54] K. Auranen, J. Uusitalo, S. Juutinen, U. Jakobsson, T. Grahn, P. T. Greenlees, K. Hauschild, A. Herzáň, R. Julin, J. Konki, M. Leino, J. Pakarinen, J. Partanen, P. Peura, P. Rahkila, P. Ruotsalainen, M. Sandzelius, J. Sarén, C. Scholey, J. Sorri, and S. Stolze, *Phys. Rev. C* **92**, 039901(E) (2015).
- [55] L. A. Bernstein, J. A. Cizewski, H.-Q. Jin, W. Younes, R. G. Henry, L. P. Farris, A. Charos, M. P. Carpenter, R. V. F. Janssens, T. L. Khoo, T. Lauritsen, I. G. Bearden, D. Ye, J. A. Becker, E. A. Henry, M. J. Brinkman, J. R. Hughes, A. Kuhnert, T. F. Wang, M. A. Stoyer, R. M. Diamond, F. S. Stephens, M. A. Deleplanque, A. O. Macchiavelli, I. Y. Lee, B. Cederwall, J. R. B. Oliveira, J. Burde, P. Fallon, C. Duyar, J. E. Draper, E. Rubel, and D. T. Vo, *Phys. Rev. C* **52**, 621 (1995).
- [56] L. G. Mann, K. H. Maier, A. Aprahamian, J. A. Becker, D. J. Decman, E. A. Henry, R. A. Meyer, N. Roy, W. Stöfl, and G. L. Struble, *Phys. Rev. C* **38**, 74 (1988).
- [57] A. Baxter, A. Byrne, G. Dracoulis, R. Bark, F. Riess, A. Stuchbery, M. Kruse, and A. Poletti, *Nucl. Phys. A* **515**, 493 (1990).
- [58] A. Poletti, G. Dracoulis, A. Byrne, A. Stuchbery, B. Fabricius, T. Kibdi, and P. Davidson, *Nucl. Phys. A* **615**, 95 (1997).
- [59] B. Fant, T. Weckström, and A. Källberg, *Physica Scripta* **41**, 652 (1990).
- [60] H. Xiaolong, *Nuclear Data Sheets* **108**, 1093 (2007).
- [61] X. Huang and M. Kang, *Nuclear Data Sheets* **133**, 221 (2016).
- [62] F. Kondev and S. Lalkovski, *Nuclear Data Sheets* **108**, 1471 (2007).
- [63] S. Zhu and F. Kondev, *Nuclear Data Sheets* **109**, 699 (2008).
- [64] N. Bijmans, P. Decrock, S. Franchoo, M. Gaeleens, M. Huyse, H.-Y. Hwang, I. Reusen, J. Szerypo, J. von Schwarzenberg, G. Vancraeynest, P. Van Duppen, and J. Wauters, *Phys. Rev. C* **58**, 754 (1998).
- [65] K. Andgren, U. Jakobsson, B. Cederwall, J. Uusitalo, T. Bäck, S. J. Freeman, P. T. Greenlees, B. Hadinia, A. Hugues, A. Johnson, P. M. Jones, D. T. Joss, S. Juutinen, R. Julin, S. Ketelhut, A. Khaplanov, M. Leino, M. Nyman, R. D. Page, P. Rahkila, M. Sandzelius, P. Sapple, J. Sarén, C. Scholey, J. Simpson, J. Sorri, J. Thomson, and R. Wyss, *Phys. Rev. C* **78**, 044328 (2008).
- [66] T. E. Cocolios, W. Dexters, M. D. Seliverstov, A. N. Andreyev, S. Antalic, A. E. Barzakh, B. Bastin, J. Büscher, I. G. Darby, D. V. Fedorov, V. N. Fedosseyev, K. T. Flanagan, S. Franchoo, S. Fritzsche, G. Huber, M. Huyse, M. Keupers, U. Köster, Y. Kudryavtsev, E. Mané, B. A. Marsh, P. L. Molkanov, R. D. Page, A. M. Sjoedin, I. Stefan, J. Van de Walle, P. Van Duppen, M. Venhart, S. G. Zemlyanoy, M. Bender, and P.-H. Heenen, *Phys. Rev. Lett.* **106**, 052503 (2011).
- [67] N. Kesteloot, B. Bastin, L. P. Gaffney, K. Wrzosek-Lipska, K. Auranen, C. Bauer, M. Bender, V. Bildstein, A. Blazhev, S. Bönig, N. Bree, E. Clément, T. E. Cocolios, A. Damyanova, I. Darby, H. De Witte, D. Di Julio, J. Diriken, C. Fransen, J. E. García-Ramos, R. Gernhäuser, T. Grahn, P.-H. Heenen, H. Hess, K. Heyde, M. Huyse, J. Iwanicki, U. Jakobsson, J. Konki, T. Kröll, B. Laurent, N. Lemesne, R. Lutter, J. Pakarinen, P. Peura, E. Piselli, L. Próchniak, P. Rahkila, E. Rapisarda, P. Reiter, M. Scheck, M. Seidlitz, M. Sferrazza, B. Siebeck, M. Sjodin, H. Tornqvist, E. Traykov, J. Van De Walle, P. Van Duppen, M. Vermeulen, D. Voulot, N. Warr, F. Wenander, K. Wimmer, and M. Zielinska, *Phys. Rev. C* **92**, 054301 (2015).
- [68] I. Hamamoto, *Nuclear Physics A* **271**, 15 (1976).
- [69] U. Jakobsson, S. Juutinen, J. Uusitalo, M. Leino, K. Auranen, T. Enqvist, P. Greenlees, K. Hauschild, P. Jones, R. Julin, S. Ketelhut, P. Kuusiniemi, M. Nyman, P. Peura, P. Rahkila, P. Ruotsalainen, J. Sarén, C. Scholey, and J. Sorri, *Phys. Rev. C* **87**, 054320 (2013).
- [70] U. Jakobsson, J. Uusitalo, S. Juutinen, M. Leino, T. Enqvist, P. Greenlees, K. Hauschild, P. Jones, R. Julin, S. Ketelhut, P. Kuusiniemi, M. Nyman, P. Peura, P. Rahkila, P. Ruotsalainen, J. Sarén, C. Scholey, and J. Sorri, *Phys. Rev. C* **85**, 014309 (2012).